Journal of Catalysis 382 (2020) 358–371

Contents lists available at ScienceDirect

Journal of Catalysis

journal homepage: www.elsevier.com/locate/jcat

Ni-Mn catalysts on silica-modified alumina for CO_2 methanation

Wilbert L. Vrijburg [a], Gabriella Garbarino [a,b], Wei Chen [a], Alexander Parastaev [a], Alessandro Longo [c,d], Evgeny A. Pidko [a,1], Emiel J.M. Hensen [a,*]

[a] Laboratory of Inorganic Materials and Catalysis, Eindhoven University of Technology, P.O. Box 513, 5600 MB Eindhoven, The Netherlands
[b] Università degli Studi di Genova, Dipartimento di Ingegneria Civile, Chimica e Ambientale, Via all'Opera Pia 15, I-16145 Genova, Italy
[c] European Synchrotron Radiation Facility, The European Synchrotron, 71 Avenue des Martyrs, 38000 Grenoble, France
[d] Istituto per lo Studio dei Materiali Nanostrutturati (ISMN)-CNR, UOS Palermo, Via Ugo La Malfa, 153, 90146 Palermo, Italy

ARTICLE INFO

Article history:
Received 1 November 2019
Revised 20 December 2019
Accepted 21 December 2019
Available online 17 January 2020

Keywords:
Methanation
Nickel
Manganese promotion
Power-to-gas
CO_2 valorization

ABSTRACT

The viability of the Power-to-Gas (PtG) concept is strongly dependent on the development of highly active and stable methanation catalysts obtained from cheap and abundant elements. In this paper, the promotional effect of MnO on Ni catalysts supported on silica-modified γ-Al_2O_3 (SA) was investigated in CO_2 and CO methanation on catalysts with Mn/Ni atomic ratios between 0 and 0.25. Significantly higher methanation rates and CH_4 selectivities were obtained for Mn-promoted compositions compared to Ni-only catalysts. The optimal NiMn/SA (Mn/Ni = 0.25) catalyst exhibited improved stability compared with unpromoted Ni/SA at 20 bar. The nature of the catalyst precursor and active catalyst was studied with STEM-EDX, XPS, and X-ray absorption spectroscopy (XAS). Evidence of a mixed Ni-Mn oxide in the catalyst precursor was obtained by EXAFS. EXAFS measurements revealed that the reduced catalyst consisted of metallic Ni particles and small oxidic Mn^{2+} species. Moreover, Mn addition improved the Ni dispersion and enhanced the Ni^{2+} reducibility by weakening the interaction between the Ni-oxide precursor and the support. A mechanistic study involving IR spectroscopy and steady-state isotopic ($^{13}CO_2$) transient kinetic analysis (SSITKA) showed that the presence of Mn enhanced CO_2 adsorption and activation.

1. Introduction

As the world transitions towards a renewable energy-based economy, major challenges involving energy storage and transportation must be addressed. The primary drawback of renewables such as wind and solar is their fluctuating and intermittent nature, which leads to the need to store substantial amounts of energy to balance short-term and long-term seasonal variations [1]. The Power-to-Gas (PtG) concept has been proposed as a strategy to store excess renewable energy in the form of synthetic natural gas [2]. PtG involves the hydrogenation of CO_2 to CH_4 with H_2 obtained from renewable energy forms, e.g. through water electrolysis using electricity from wind and solar. The advantages of synthetic natural gas are high energy density and compatibility with the current energy infrastructure, which includes an efficient grid for distribution [3–5].

The methanation of CO_2, also known as the Sabatier reaction, proceeds as follows:

$$CO_2 + 4H_2 \rightleftharpoons CH_4 + 2H_2O \qquad \Delta H_{298} = -165\,\mathrm{kJ/mol} \tag{1}$$

Catalysts are required to obtain sufficiently high rates and selectivities for practical implementation of the PtG technology [6,7]. Although methanation catalysts have already been investigated for a long time, there remains a specific need to develop cheaper catalysts with a high activity at low temperature [2]. Among the transition metals investigated, Ru shows the highest CO_2 methanation activity and CH_4 selectivity [8–13]. Large-scale industrial application of Ru catalysts is hindered by the relatively high cost of this transition metal. For this reason, cheaper Ni-based catalysts dispersed on Al_2O_3 are preferred for commercial implementation of methanation processes. The high dispersion of Ni on γ-Al_2O_3 can also lead to active and selective catalysts [14,15]. A specific drawback in obtaining practical Ni-based Sabatier catalysts is the higher rate of deactivation, which is due to the tendency of carbon deposition as well as Ni sintering at the higher loadings required to achieve high activity [3,5]. Bimetallic systems have been studied in order to improve the activity and

* Corresponding author.
E-mail address: e.j.m.hensen@tue.nl (E.J.M. Hensen).
[1] Present address: Inorganic Systems Engineering group, Department of Chemical Engineering, Delft University of Technology, Van der Maasweg 9, 2629 HZ, Delft, The Netherlands.

https://doi.org/10.1016/j.jcat.2019.12.026
0021-9517/

stability of Ni-based catalysts. Most of these studies have focused on the addition of noble metal promotors such as Pt, Pd and Ru to Ni-based catalysts [16,17]. It would be desirable however to find other cheaper base metal promoters for Ni. For instance, the use of Fe and Co as promoters for Ni-based CO_2 methanation catalysts led to higher CH_4 yields in comparison with their monometallic counterparts [18,19]. Mn is another promoter that has earlier received attention in the context of Fischer-Tropsch synthesis for NiMn [20] and CoMn catalysts [21–24]. Earlier reports also showed that the addition of Mn to Ni/Al_2O_3 can increase CO/CO_2 methanation rates, which was attributed to a higher Ni dispersion in the presence of Mn [25–27]. The group of Stockenhuber studied the influence of Mn and other transition metals on Ni/Al_2O_3 catalysts using NO IR spectroscopy and found that Mn addition increased the number of electron accepting sites, which facilitated CO activation [28]. Burger *et al.* used co-precipitation to prepare $NiMn/Al_2O_3$ catalysts with an increased amount of medium basic sites, which resulted in a higher CO_2 adsorption capacity and increased catalytic activity [29,30]. The same explanation was put forward in the work of Zhao *et al.*, who also promoted Ni/Al_2O_3 with Mn [27]. There is ample room for improvement of such Ni/Al_2O_3, for instance with respect to the undesired formation of Ni-aluminate ($NiAl_2O_4$) species, which can only be reduced at temperatures above 750 °C to metallic Ni [31].

Despite these earlier works, there is no clear understanding about the synergy between Ni and Mn for the Sabatier reaction. In our recent model study, we used TiO_2-supported NiMn catalysts to investigate in detail this Ni-Mn synergy for CO_2 and CO hydrogenation [32]. We established that the interface between small Mn-oxide clusters dispersed on metallic Ni and metallic Ni itself are the active sites for C-O bond dissociation in CO_2 and CO. Hydrogenation of the resulting CH_x species occurs on the metallic Ni surface. An important aspect of the proposed mechanism is the formation of oxygen defects in the Ni-supported Mn-oxide clusters, which give rise to the formation of H_2O. Due to the strong interaction between Mn and TiO_2, a significant part of the Mn promoter did not interact with the metallic Ni nanoparticles upon reduction in these $NiMn/TiO_2$ catalysts, which most likely led to a suboptimal promotion of Ni by Mn.

In the present study, we focused on Al_2O_3 as a support for NiMn-based catalysts for CO_2 methanation with the aim to improve the Ni-Mn synergy by lowering the metal-support interactions. The formation of $NiAl_2O_4$ was suppressed by using a silica-modified alumina (SA) support. Catalysts were prepared at varying Mn/Ni ratio to identify the optimum composition and to understand the Ni-Mn synergy in more detail. For this purpose, we characterized the catalysts by XPS, X-ray absorption spectroscopy (XAS), *in situ* IR spectroscopy and STEM-EDX mapping. We also used steady-state isotopic transient kinetic analysis to understand the reaction mechanism.

2. Experimental methods

2.1. Catalyst preparation

SIRAL20 is a silica-modified boehmite obtained from Sasol. The precursor SIRAL20 was calcined at 550 °C (5 °C/min, 3 h) prior to impregnation. $Ni(NO_3)_2{\cdot}6H_2O$ (99.9%) and $Mn(NO_3)_2{\cdot}4H_2O$ (99.9%) were obtained from Sigma Aldrich and used without further purification. Catalysts were prepared using conventional incipient-wetness impregnation (IWI). $Ni(NO_3)_2{\cdot}6H_2O$ (2.97 g) and $Mn(NO_3)_2{\cdot}4H_2O$ (0–0.64 g) were simultaneously dissolved in an appropriate amount of deionized H_2O and added dropwise to calcined SIRAL20 (denoted as SA, ca. 2.5 g). Catalysts were dried overnight at 110 °C and calcined in air at 350 °C (5 °C/min, 3 h).

2.2. Characterization

Elemental analysis. The metal content of as-synthesized materials was determined by ICP-OES (Spectro Blue ICP). Samples (25 mg) were dissolved in 1.5 mL acid solution composed of equimolar HF, HNO_3, and H_2O, and 5 mL concentrated H_2SO_4 at 250 °C.

X-ray diffraction (XRD). The crystal structure of the metal nanoparticles and the crystallinity of the support were studied using XRD. Powder XRD patterns were recorded on a Bruker D2 Phaser diffractometer using CuK_α radiation with a wavelength of 1.54 Å. The 2θ angles were measured between 10 and 80° with a step size of 0.02° at 1.0 s/step.

H_2 chemisorption. H_2 chemisorption was performed using a Micromeritics ASAP 2020. Typically, 50 mg catalyst was loaded into a quartz U-tube reactor and reduced at 550 °C (5 °C/min, 4 h), evacuated at 570 °C to remove chemisorbed species prior to H_2 chemisorption at 35 °C.

Temperature-programmed reduction (TPR). H_2-TPR experiments were performed using a Micromeritics Autochem II 2920 equipped with a fixed-bed U-tube reactor, furnace, and thermal conductivity detector (TCD). Typically, 50 mg catalyst was loaded in a quartz reactor. H_2-TPR was carried out in 4% H_2 in N_2 at 50 mL/min between 50 and 1000 °C at 10 °C/min. The H_2 signal was calibrated using a CuO/SiO_2 reference catalyst.

Scanning transmission electron microscopy energy-dispersive X-ray spectroscopy (STEM-EDX). Particle sizes and elemental distribution was studied using STEM-EDX. Measurements were obtained using an FEI cubed Cs corrected Titan operating at 300 kV. Samples were crushed, sonicated in ethanol and dispersed on a holey Cu support grid. Elemental analysis was done with an Oxford Instruments EDX detector X-Max^N 100TLE. Carbon contamination during elemental mapping acquisition led to each area to be measured only once.

X-ray photoelectron spectroscopy (XPS). The surface elemental composition of calcined and reduced materials was analyzed by XPS. Finely crushed samples were placed on double-sided carbon tape and analyzed using a K-Alpha XPS apparatus (Thermo Scientific). Spectra were obtained using an Al anode (Al Kα = 1486.68 e V) with 50 scans in the Ni 2p and Mn 3p region. The Mn 2p region overlaps considerably with the Ni Auger region and is therefore not appropriate to determine Mn content or oxidation state. To deconvolute the contributions of Ni 3p and Ni 3s from the Al 2p and Al 2s regions, respectively, scans were performed between 40 and 130 eV (Mn 3p to Al 2s regions) and fitting models were employed with appropriate constraints. Reduced catalysts were prepared under inert conditions in an N_2 glovebox and transferred to the XPS apparatus using a custom-built air-tight transport vessel. All spectra were analyzed with CasaXPS, charge corrected against the C 1s binding energy of adventitious carbon at 284.8 eV, and were fitted using a Shirley background.

X-ray absorption spectroscopy (XAS). The reduction and structure of the catalysts were studied using *operando* XAS. Data was collected at the Ni K-edge (8.3 keV) and Mn K-edge (6.5 keV) in transmission mode at the Dubble BM26A beamline at ESRF, Grenoble, France. The energy was selected with a Si (1 1 1) monochromator and calibrated with Ni (E_0 = 8333 eV) and Mn (E_0 = 6539 eV) foil, respectively. Collected XAFS data were background subtracted, normalized, and fitted using linear combination fitting (LCF) as implemented in the Athena software package [33]. At the Ni K-edge, the fresh (calcined) sample and the Ni foil served as references for the oxidized and metallic state of the catalyst for LCF. At the Mn K-edge, the Mn oxidation state was estimated from the energy at the half-edge jump. Linear regression of reference XANES spectra from MnO_2, Mn_3O_4, Mn_2O_3, MnO(OH), and MnO were used to correlate half-edge jump energies to the Mn oxidation state. EXAFS analysis on k^3-weighted Ni K-edge data

was performed with Artemis. Scattering paths were calculated with FEFF6 using relevant crystal structures [33]. The amplitude reduction factor S_0^2 was determined by fitting the first and second shell Ni-O and Ni-Ni coordinations to 6 and 6 respectively of a β-$Ni(OH)_2$ reference sample at the Ni K-edge (8.3 keV). EXAFS analysis for Mn K-edge measurements was performed with Viper. Likewise, S_0^2 for Mn was determined by fitting the first two shells (Mn-O and Mn-Mn, respectively) of a MnO reference sample at the Mn K-edge (6.5 keV).

In a typical *in situ* experiment, ca. 30 mg catalyst (75–125 μm) and 100 mg boron nitride (75–125 μm) were physically mixed and loaded in a quartz tube (250 mm length, 4 mm i.d., 5 mm o.d., with a 20 mm flattened region with a thickness of 0.1 mm per wall). Quartz wool was used to plug both sides of the catalyst bed. Catalysts were reduced *in situ* at 550 °C (5 °C/min, 1 h) under 20% H_2 in He flow at 50 mL/min and returned to room temperature. Catalysts were exposed to CO_2/H_2/He gas mixture 2.5/10/37.5 mL/min ratio and heated to 300 °C (5 °C/min, 1 h) and returned to room temperature. Methane production was monitored by mass spectrometry (OmniStar GSD 320 instrument). Temperature-programmed reactions (e.g. reduction, CO_2 hydrogenation) were performed whilst recording XANES spectra, while EXAFS spectra were recorded at RT (below 50 °C) before and after reactions. In order to obtain a sufficient signal-to-noise ratio, Mn K-edge measurements were carried out in a stainless-steel XAS reactor equipped with two fire-rods and glassy carbon windows (thickness = 0.5 mm) as described elsewhere [34]. The maximum temperature was limited to 500 °C by the thermal stability of the polyimide resin used to glue the glassy carbon windows to the steel window holders.

Infrared spectroscopy (IR). *In situ* IR spectroscopy was performed on a Bruker Vertex 70v Fourier transform infrared spectrometer equipped with a DTGS detector. Averaged spectra were collected using 32 scans with a resolution of 2 cm^{-1} between 4000 and 1000 cm^{-1}. Samples were pressed into wafers of 15 mg, placed in an environmental transmission cell equipped with CaF_2 windows and reduced *in situ* at 550 °C (5 °C/min, 1 h) under H_2/N_2 flow. Samples were then outgassed at 300 °C for 30 min to remove surface contaminants, followed by cooling to 50 °C under vacuum prior to introducing other gases. CO_2 was administered by using a 10 μL sample loop connected to a six-way valve. Adsorption was studied up to pressure of 10 mbar CO_2. Temperature-programmed desorption (TPD) was employed to study the evolution and removal of adsorbed species. The sample was heated to 350 °C (5 °C/min) whilst collecting spectra at intervals of 25 °C. For *in situ* methanation measurements, reduced catalysts were exposed at 50 °C to an atmosphere of 100 mbar composed of H_2 and CO_2 at a H_2/CO_2 molar ratio of 4. The sample was heated to 350 °C (5 °C/min) and spectra were recorded at intervals of 25 °C.

2.3. Catalytic activity measurements

CO_2 hydrogenation. The catalytic performance in CO_2 hydrogenation was determined between 200 and 400 °C in a parallel 10-flow high-throughput reactor setup. Typically, 50 mg of catalyst (75–125 μm sieved fraction) and 150 mg SiC was loaded in a quartz reactor tube. Catalysts were reduced *in situ* at 550 °C (5 °C/min, 4 h) under 10 vol% H_2/He at 50 mL/min. The reaction mixture (50 mL/min total flow, 5 vol% CO_2, 20 vol% H_2, balance He) was introduced at 200 °C, and the reactor effluent was analyzed every 25 °C until 400 °C. Steady-state activities were generally obtained after 25 min.

High-pressure CO_2 hydrogenation experiments were performed at a total pressure of 20 bar. Typically, an amount of 200 mg catalyst (75–125 μm sieve fraction) was loaded in a stainless-steel flow reactor. Catalysts were reduced at 550 °C (5 °C/min, 4 h) under 20 vol% H_2 in He at 50 mL/min. The reaction mixture (50 mL/min total flow, 20 vol% CO_2, 80 vol% H_2) was introduced into the reactor at 200 °C. The reactor effluent was analyzed every 25 °C until 300 °C. Catalyst stability was studied at 300 °C for 24 h.

CO hydrogenation. The catalytic activity in CO hydrogenation was evaluated between 250 and 450 °C in a parallel 10 reactor high-throughput setup. 25 mg catalyst (75–125 μm sieve fraction) and 150 mg SiC was loaded in each quartz reactor. Catalysts were reduced *in situ* at 550 °C (5 °C/min, 4 h) under 10 vol% H_2/He at 50 mL/min. The reaction mixture (50 mL/min total flow, 7 vol% CO, 42 vol% H_2, balance He) was introduced at 250 °C, and the reactor effluent was analyzed every 25 °C until 450 °C. An excess H_2 with respect to CO was employed to avoid catalyst deactivation through carbon deposition.

Products were analyzed by online GC (Interscience CompactGC) equipped with Restek Rt-Q-Bond and Rt-Msieve 5 Å (TCD), Restek Rt-U-Bond and Rt-Q-Bond (TCD), and Restek Rtx-1 (FID) columns. The CO_2 conversion (X_{CO2}), and CH_4 (S_{CH4}) and CO (S_{CO}) selectivities are calculated as:

$$X_{CO_2} = \frac{[CH_4] + [CO]}{[CO_2] + [CH_4] + [CO]} \quad (4)$$

$$S_{CH_4} = \frac{[CH_4]}{[CH_4] + [CO]} \quad (5)$$

$$S_{CO} = \frac{[CO]}{[CH_4] + [CO]} \quad (6)$$

No other hydrocarbons than CH_4 were observed. For CO methanation activity measurements, CO conversion (X_{CO}), and CH_4 (S_{CH4}) and CO_2 (S_{CO2}) selectivities are calculated as:

$$X_{CO} = \frac{[CH_4] + [CO_2] + [C_2] + [C_3]}{[CO_2] + [CH_4] + [CO] + [C_2] + [C_3]} \quad (7)$$

$$S_{CH_4} = \frac{[CH_4]}{[CH_4] + [CO_2] + [C_2] + [C_3]} \quad (8)$$

$$S_{CO_2} = \frac{[CO_2]}{[CH_4] + [CO_2] + [C_2] + [C_3]} \quad (9)$$

Very small amounts of C_2 and C_3-products were observed, which are not discussed further.

Steady-state isotopic transient kinetic analysis (SSITKA). The setup used for SSITKA measurements is described in detail in a previous work [35]. For a typical measurement, 50 mg catalyst was loaded into reactor and diluted by SiC. *In situ* reduction was performed in a diluted H_2 flow (20 vol% H_2 in Ar, 50 mL/min in total) at 550 °C (T_{ramp} = 5 °C/min) and atmospheric pressure for 2 h. The reactor was subsequently cooled in dilute H_2 flow to 200 °C followed by an increase of the pressure to 2 bar. The reaction was started by a forward transient switch (from H_2/He = 10/3.5 mL/m in to H_2/CO_2/Ar = 10/2.5/1 mL/min) followed by an isothermal dwell for 2 h in order to obtain steady-state, which was evaluated by an online GC (Thermo Scientific, Trace GC 1300). An extra Ar flow was fed to keep total flow rate at 50 mL/min. The SSITKA was performed by switching from $H_2/^{12}CO_2$/Ar to $H_2/^{13}CO_2$/He. The transient of $^{13}CO_2$ (m/z = 45), $^{12}CO_2$ (m/z = 44), $^{13}CH_4$ (m/z = 17), $^{12}CH_4$ (m/z = 15) and He (m/z = 4) were recorded by online mass spectrometry (EES, GeneSys).

3. Results and discussion

As support material, we used silica-stabilized alumina (SA) containing 20 wt% SiO_2 on high-purity Al_2O_3. The SIRAL20 precursor was calcined at 550 °C before catalyst preparation. The γ-Al_2O_3 phase can effectively disperse the Ni phase and can achieve small

particles after reduction, while the silica component increases the (hydro)thermal stability of γ -Al_2O_3 against sintering. Modifying the alumina surface with silicon species also lowers the interaction with Ni, decreasing the formation of poorly reducible $NiAl_2O_4$ [31]. The BET surface area and pore volume of the calcined support were 369 m^2/g and 0.9 mL/g, respectively. Nitrate salts of Ni and Mn were used for (aqueous) incipient wetness impregnation of the SA support. The physico-chemical properties of the calcined catalysts are collected in Table 1. Mn/Ni ratios were between 0 and 0.25 with the Ni loading for all catalysts being nearly similar at ~ 17 wt%. The XRD patterns of the calcined samples (Fig. 1a) showed NiO reflections (JCPDS no.: 047–1049) at 2θ = 37.3° (1 1 1), 43.3° (2 0 0) and 62.9° (2 2 0) for all Ni catalysts. Broad reflections from the γ-Al_2O_3 at 2θ = 45.7° (1 1 1) and 66.6° (2 1 1) overlapped with some of the NiO reflections. The absence of a shift in the reflection at 66.6° of Al_2O_3 indicated that no significant amounts of $NiAl_2O_4$ had formed during calcination. The absence of reflections due to Mn-oxide phases points to a good dispersion of Mn. We did not find a systematic shift in the NiO reflections, reflections in the Ni-based catalysts indicates that the addition of Ni helps to disperse the Mn phase, which may suggest that a mixed NiMn oxide did not form. Calcined Mn/SA shows sharp reflections at 2θ = 28.7° (1 1 0), 37.3° (1 0 1), 42.8° (1 1 1), 56 0.7° (2 1 1), 59.4° (2 2 0), and 72.3° (3 0 1) assigned to β-MnO_2 (JCPDS no. 024–0735). The XRD patterns of reduced and passivated catalysts (Fig. 1b) show predominantly contributions of metallic Ni at 2θ = 44.5° (1 1 1), 51.8° (2 0 0), and 76.3° (2 2 0) (JCPDS no. 04–0850). Minor contributions from NiO can be discerned, which is likely due to sample passivation. No shift was found in the Ni peak positions, indicating that Mn is not incorporated in the metallic Ni particles. No contributions from bulk oxidic or reduced Mn phases were observed in the reduced NiMn catalysts. The XRD pattern of the reduced Mn/SA catalysts only contained MnO reflections (JCPDS no.: 07–0230) at 2θ = 34.9° (1 1 1), 40.5° (2 0 0), 58.7° (2 2 0), 70.2° (3 1 1), and 73.8° (4 0 0), indicating that MnO cannot be reduced. By applying the Scherrer equation to the Ni(2 0 0) reflection at 2θ = 51.8°, average Ni particle sizes were estimated to be in the 5–11 nm range. In comparison to Ni/SA, the addition of Mn resulted in a higher Ni dispersion upon reduction. The higher Ni dispersion is in keeping with the larger number of H_2 chemisorption sites (Table 1).

H_2-TPR profiles of the catalysts are shown in Fig. 2. For all Ni catalysts, temperatures above 700 °C are required to fully reduce the Ni with maximum hydrogen uptake between 550 and 600 °C. The reduction of alumina-supported Ni catalysts depends on the nature and strength of the interaction between Ni-oxide and the alumina support [36]. From the obtained TPR profiles, we can deduce that there are contributions of both bulk NiO reduction at 400 °C, and more dispersed NiO interacting with the alumina support between 500 and 800 °C [37,38]. Bulk Mn/SA reduction leads to two hydrogen consumption features, corresponding to the reduction of MnO_2 to Mn_3O_4 at 375 °C, followed by reduction to

Table 1
Textural and structural properties of SiO_2-Al_2O_3 (SA) supported catalysts.

Sample	Ni wt%	Mn wt%	Mn/Ni	S.A. (m^2/g)[1]	d (nm, XRD)	d (nm, H_2 chem.)	d (nm, TEM)	H_2 chem. (mmol/g)[2]
SA	n/a	n/a	n/a	369				n.m.[3]
Ni/SA	17.7	0	0	273	10.7	8.3	12.5	0.183
NiMn(0.05)/SA	17.9	0.8	0.05	257	8.6	7.3	6.4	0.210
NiMn(0.1)/SA	16.7	1.6	0.10	277	5.6	6.5	5.7	0.220
NiMn(0.2)/SA	17.3	3.0	0.19	276	6.5	7.1	5.6	0.210
NiMn(0.25)/SA	16.8	4.0	0.25	274	8.4	6.3	6.9	0.230
Mn/SA		16.9		248	30.1			0

[1] Surface area determined by BET method.
[2] H/Ni = 1 assumed.
[3] Not measured.

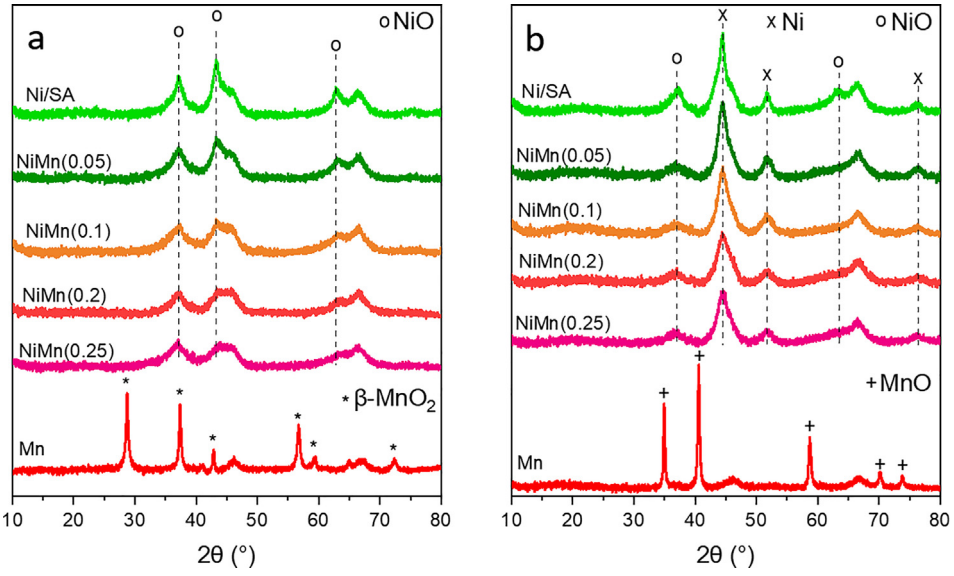

Fig. 1. XRD patterns of (a) calcined and (b) reduced Ni, NiMn, and Mn catalysts supported on SA. Reduced catalysts were passivated at room temperature before recording XRD patterns.

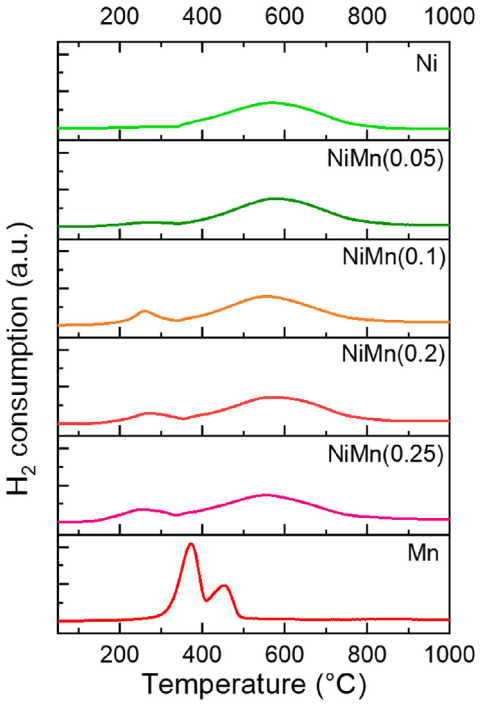

Fig. 2. H_2-TPR profiles of Ni, NiMn, and Mn supported on SA.

MnO at 450 °C [39]. For NiMn catalysts, contributions from manganese reduction were observed at lower temperatures with a hydrogen consumption feature around 260 °C. This indicates a clear interaction between the Ni and Mn oxidic phases.

The proximity of the Ni and Mn oxide phases in calcined catalysts was further explored with STEM-EDX. HAADF-STEM images with EDX mapping of Ni/SA after calcination (Fig. 3) show that Ni is well dispersed over the support. Nevertheless, nickel oxide platelets observed in HAADF-STEM evidence the proximity of Ni and Al in EDX maps. These data support the stronger interaction of Ni with the alumina than with the silica part. In contrast, while calcined NiMn(0.25) (Fig. 4) also showed the presence of nickel oxide platelets, the EDX map revealed that these platelets contained both Ni and Mn. This indicates the formation of a mixed NiMn-oxide phase, highlighting the close proximity between Ni and Mn before reduction at some locations.

Following reduction at 550 °C, Ni nanoparticles were formed, while the Mn remained uniformly distributed over the support with no clear affinity for the Ni nanoparticles (Supporting Information, Figures S2-S5). Particle size distributions determined by HAADF-STEM (Fig. 5) confirmed that NiMn catalysts led to smaller and more uniformly dispersed nanoparticles than Ni catalysts. Average particle sizes decreased from 12.5 nm for Ni/SA to between 5.5 and 7.0 nm for Mn-containing catalysts. Nevertheless, HAADF-STEM measurements did not evidence a clear trend of smaller particles for higher Mn/Ni ratio (Table 1).

Although we cannot determine a clear affinity between Ni and Mn in the reduced catalysts from our EDX maps (Supporting info, Figures S2-S5), we use XPS to show that part of Mn is associated with Ni at the Ni nanoparticle level. For this purpose, we determined the Mn/Ni surface ratios before and after reduction (Table 2). When compared with the bulk Mn/Ni ratios determined by elemental analysis, the XPS Mn/Ni ratios are consistently higher in both the calcined and the reduced catalysts. Relatively speaking, this implies a higher dispersion of Mn, and thus supports a model where Mn decorates Ni in the reduced catalyst.

CO_2 hydrogenation was employed to examine the influence of Mn on the methanation activity of Ni/SA based catalysts. CO_2 conversion was measured in a high-throughput flow setup between 200 and 400 °C and at atmospheric pressure (Fig. 6a). The main product on the Ni-containing catalysts was CH_4 with minor amounts of CO above 250 °C (Fig. 6b). The Mn/SA catalyst was completely inactive towards hydrogenation products, although small quantities of CO were observed at elevated temperature. Mn-promoted Ni-based catalysts all showed increased CO_2 methanation activity compared to Ni/SA. The promotional effect increased with higher Mn/Ni ratio. The thermodynamics of exothermic CO_2

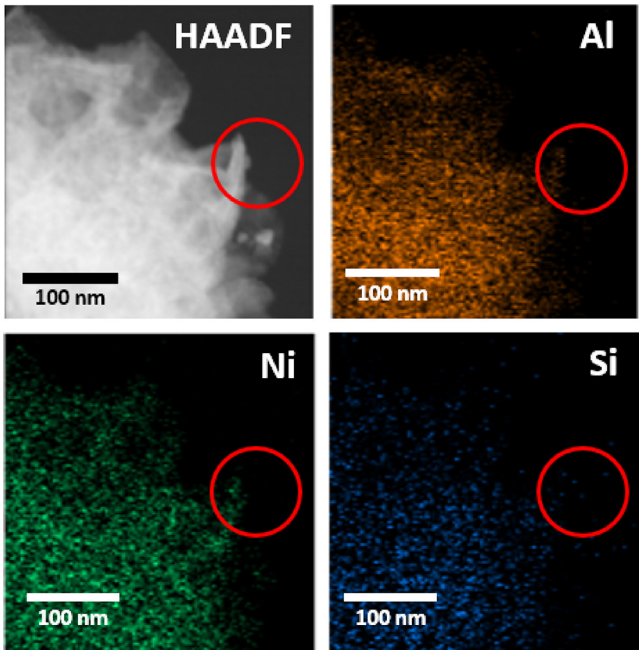

Fig. 3. HAADF-STEM and EDX mapping images of calcined Ni/SA. The inset shows an alumina-rich region, likely rod-shaped from the boehmite precursor, which is low in Si and rich in Ni, indicating the strong affinity between Ni and alumina.

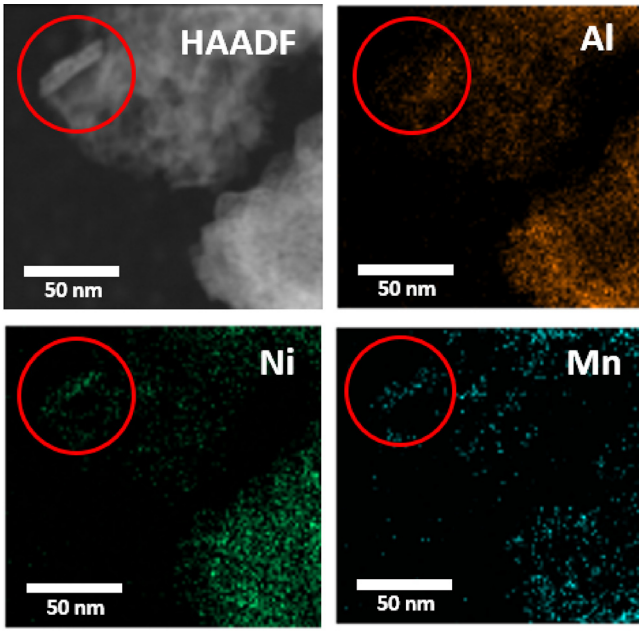

Fig. 4. HAADF-STEM and EDX mapping of calcined NiMn(0.25)/SA catalyst.

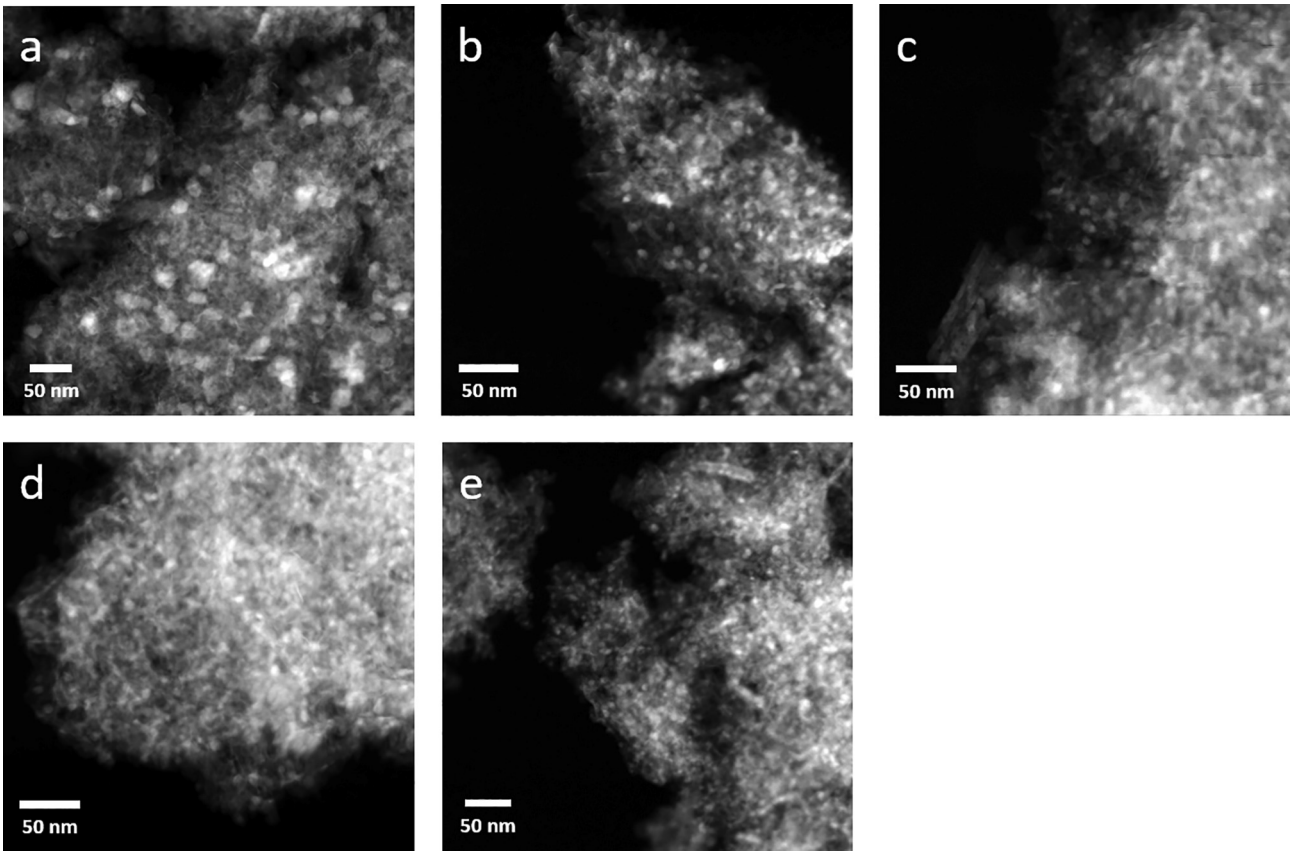

Fig. 5. HAADF-STEM images of (a) Ni/SA, (b) NiMn(0.05)/SA, (c) NiMn(0.1)/SA, (d) NiMn(0.2)/SA, and (e) NiMn(0.25)/SA catalysts after reduction at 550 °C.

Table 2
Atomic surface ratios as determined by XPS analysis of the Si 2p, Al 2p, Ni $2p_{3/2}$, and Mn 3p regions.

Sample	Si/(Si + Al) Calcined	Reduced	Mn/Ni Calcined	Reduced
Ni/SA	0.19	0.21		
NiMn(0.05)/SA	0.20	0.22	0.09	0.23
NiMn(0.1)/SA	0.22	0.22	0.16	0.30
NiMn(0.2)/SA	0.20	0.22	0.29	0.49
NiMn(0.25)/SA	0.20	0.21	0.31	0.51
Mn/SA	0.21	0.21		
SA	0.21			

methanation meant most active NiMn catalyst reached a close-to-equilibrium conversion around 350 °C, beyond which overall conversion decreased. An assessment of the catalyst stability at 300 °C revealed that all catalysts were stable during 40 h (Fig. 6c). Moreover, the most active NiMn/SA catalysts also exhibited a significantly lower CO selectivity than Ni/SA during the stability test at 300 °C (Supporting Information, Figure S6). TOFs normalized by surface Ni were determined under differential conditions (<10% CO_2 conversion) and showed a more than 3-fold increase in methanation activity at a reaction temperature of 200 °C (Table 3). Recent studies highlighted the structure-sensitive nature of CO_2 methana-

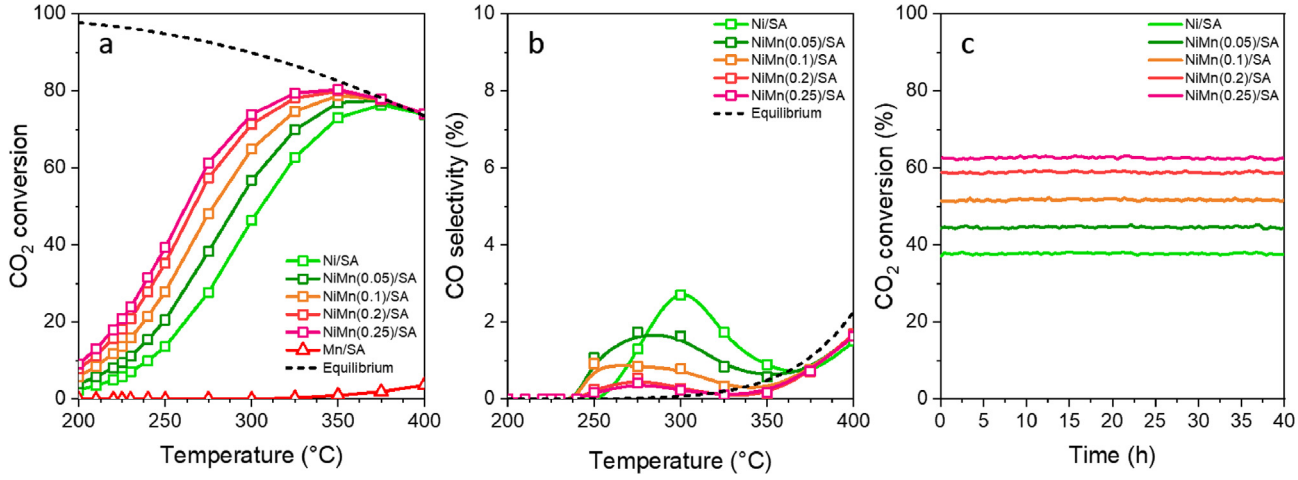

Fig. 6. Comparison of CO_2 methanation for Ni/SA, NiMn/SA and Mn/SA catalyst (50 mg, $H_2/CO_2 = 4$) highlighting (a) steady-state CO_2 conversion between 200 and 400 °C, (b) CO selectivity during CO_2 methanation, and (c) stability at 300 °C over 40 h.

Table 3
Turnover frequencies at 200 °C and apparent activation energies.

Sample	TOF, 10^{-3} mol CH_4/mol surface Ni/s	E_{act}^{app}, kJ/mol (±)
Ni/SA	2.25	71.8 (0.5)
NiMn(0.05)/SA	3.26	67.7 (0.5)
NiMn(0.1)/SA	4.63	64.8 (0.7)
NiMn(0.2)/SA	6.36	63.9 (0.8)
NiMn(0.25)/SA	6.81	62.3 (0.8)
Mn/SA	0	n/a

tion over silica-supported catalysts [40], whilst others reported that this reaction is structure insensitive on Ni/Al_2O_3 [41]. Despite the larger particles obtained for Ni/SA, we cannot attribute the increase in TOFs to the higher Ni dispersion observed on Mn-promoted catalysts, because all promoted catalysts have near-identical Ni particle sizes. Instead, the TOF trend follows the Mn/Ni ratio. The increase in TOF between NiMn(0.2) and NiMn(0.25) is relatively small, suggesting that the optimum Mn/Ni ratio is close to these values. We expect that a higher Mn/Ni ratio may provide a further small improvement in methanation activity, although such compositions were not explored in this study.

From the TOF values between 200 and 240 °C, we constructed Arrhenius plots (Supporting Information, Figure S7) and calculated activation energies (Table 3). The addition of Mn led to a decrease of the apparent activation barrier for CO_2 methanation from 72 kJ/mol for Ni/SA to 62 kJ/mol for NiMn(0.25). This might be due to a change in the mechanism. Considering the lack of hydrogenation activity from Mn/SA, we speculate that Mn addition facilitates the activation of CO_2. Overall, the apparent activation barriers of promoted catalysts compare favorably with those reported in literature [42,43]. We also investigated whether Mn displayed synergy with Ni in the methanation of CO. The results indicate a similar promotion for CO methanation as observed for CO_2 methanation (Supporting Information, Figure S8), consistent with earlier findings for TiO_2-supported NiMn catalysts [32].

The optimal NiMn catalyst was then employed in high-pressure CO_2 methanation at 20 bar, as these conditions are more close to future PtG scenarios. Fig. 7a shows that the promotional effect of Mn is also apparent at a reaction pressure of 20 bar. Under these conditions, the catalysts only produced CH_4. Following a 24 h stability test, we found that Ni/SA lost almost 18% of its initial activity at 300 °C, whereas NiMn(0.25)/SA deactivated by<5%, highlighting its superior activity and stability (Fig. 7b).

To obtain a more comprehensive understanding about the chemical environment of the Ni and Mn in the active catalysts, selected samples were studied using *operando* XANES. Fig. 8 shows Ni K-edge spectra obtained for Ni/SA and NiMn(0.25)/SA during reduction up to 550 °C. Linear combination fitting (LCF) was employed to estimate the degree of reduction by using the spectra of calcined catalysts and Ni foil as references for Ni^{2+} and metallic Ni, respectively. By comparing the temperature-programmed reduction LCF of Ni/SA (Fig. 8a, middle) and NiMn(0.25)/SA (Fig. 8b, middle), we observed that Mn addition clearly improved the reducibility of the Ni. Specifically, LCF results highlight that the onset of reduction (estimated using Ni^{2+}/Ni^0 = 1) was approximately 85 °C lower for NiMn/SA catalysts compared with Ni/SA. However, the improved reducibility only had a marginal impact on the final Ni reduction degree with Ni/SA and NiMn(0.25)/SA, respectively, containing 93% (Fig. 8a, right) and 96% (Fig. 8b, right) metallic Ni after 80 min at 550 °C. The improved Ni reducibility in Mn-promoted catalysts can be linked to the formation of a mixed NiMn-oxide phase, which lowers the interaction of Ni with the alumina support, therefore corroborating the STEM-EDX results. Still, the incomplete reduction of both catalysts indicates that a fraction of the Ni remains in a strong interaction with Al_2O_3. Thus, a higher Mn/Ni ratio may be beneficial to reach an optimum promotional effect.

The evolution of Mn during catalyst activation was followed with XANES in a similar manner (Fig. 9). Mn can exhibit redox states between 0 and +7 of which +2, +3, and +4 are most commonly observed. Determining the Mn oxidation state is challenging [44,45]. Therefore, the evolution of the Mn oxidation state during reduction of Mn/SA and NiMn(0.25)/SA was estimated by the edge energy at half the edge jump calibrated against reference compounds, which provides a linear correlation between the Mn oxidation state and the edge position (Supporting information) [45,46]. The evolution of Mn oxidation state during reduction is presented in Fig. 9c. In the absence of Ni, Mn/SA begins as tetravalent Mn, which is consistent with the XRD identification of β-MnO_2 upon calcination. Reduction starts around 250 °C, which yields a mixed Mn^{3+}/Mn^{2+}-oxide by 350 °C attributable to Mn_3O_4 [29,39]. Deeper

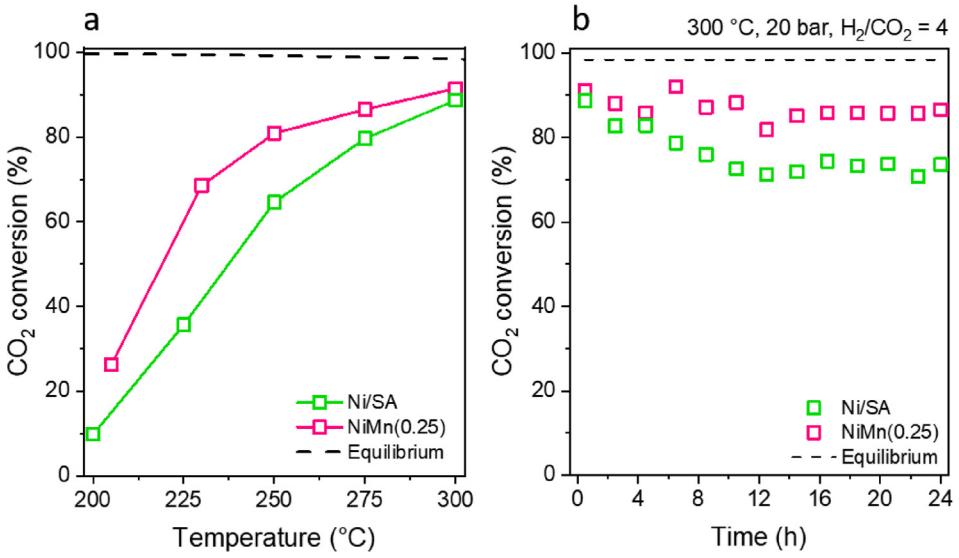

Fig. 7. High-pressure (20 bar) CO_2 methanation (a) between 200 and 300 °C and (b) stability at 300 °C for 24 h. Measurements were performed using 200 mg catalyst at 20 bar in a stoichiometric H_2/CO_2 gas mixture.

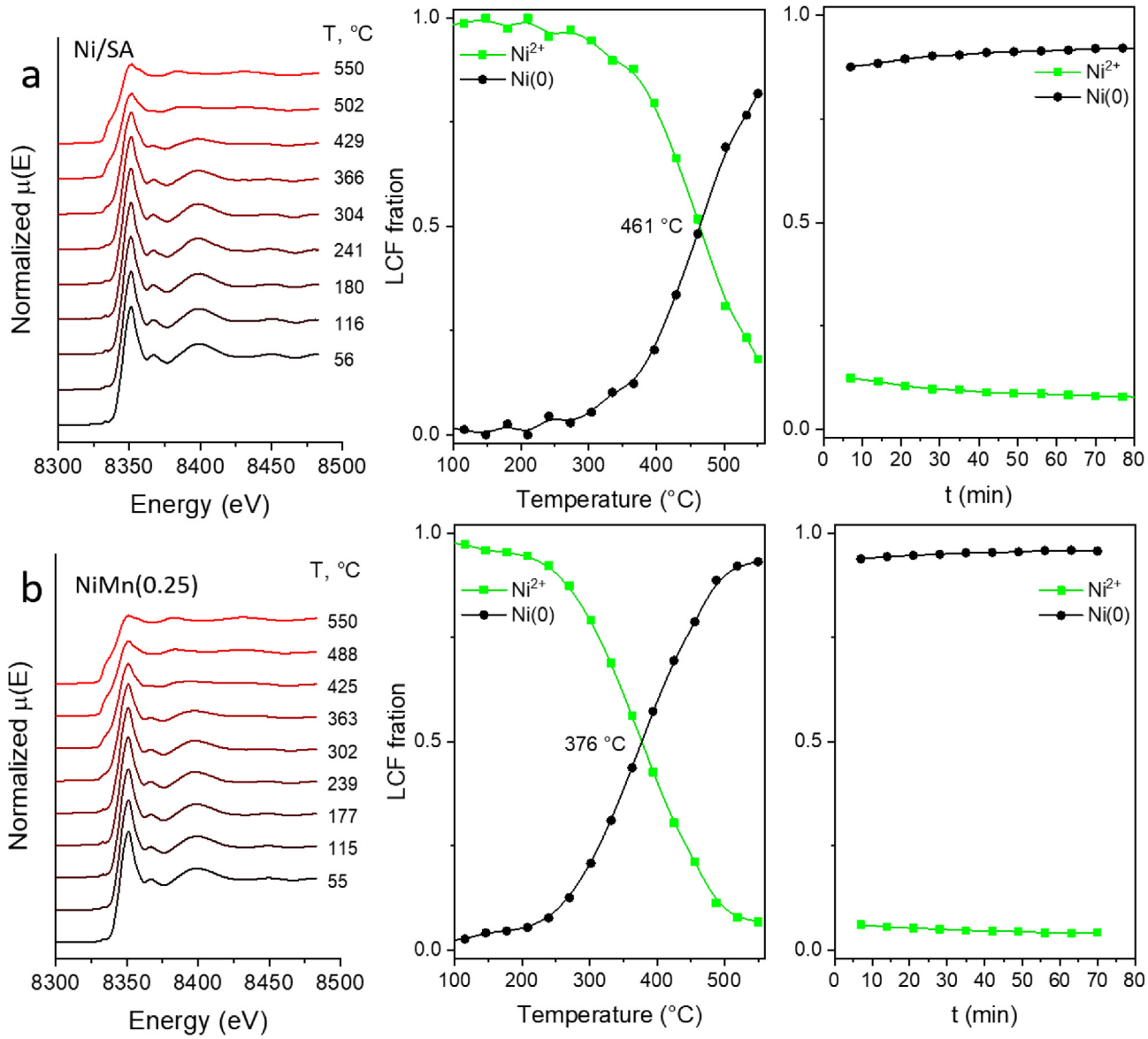

Fig. 8. Ni K-edge measured XANES spectra of (a, left) Ni/SA and (b, left) NiMn(0.25)/SA during reduction between room temperature and 550 °C. The degree of Ni reduction during the temperature ramp for (a, middle) Ni/SA and (b, middle) NiMn(0.25)/SA. Reduction degree during 80 min dwell at 550 °C for (a, right) Ni/SA and (b, right) NiMn (0.25)/SA. Reduction degrees were estimated using LCF of calcined Ni/SA and Ni foil as references for oxidized and reduced Ni.

reduction to Mn^{2+} is achieved by 400 °C. In contrast, NiMn(0.25)/SA begins as a mixed Mn^{4+}/Mn^{3+}-oxide, and follows a more gradual reduction profile to either a Mn^{3+} or a mixed Mn^{3+}/Mn^{2+}-oxide around 200 °C, followed by further reduction to Mn^{2+} by 300 °C. Combining Ni and Mn K-edge XANES data shows that for NiMn (0.25)/SA, nearly all Mn is reduced to the +2 oxidation state prior to the onset of Ni reduction, and that the presence of Ni facilitates Mn reduction.

Structural information about the active phase was obtained with EXAFS on the Ni and Mn K-edges. EXAFS spectra obtained on the Ni K-edge were background subtracted in Athena, and fitted in Artemis using single scattering paths calculated with FEFF6. Table 4 summarizes the path distances and coordination numbers determined for calcined and reduced catalysts on the Ni K-edge. The k^3-weighted Fourier-transformed EXAFS spectra (not phase corrected) are plotted in R-space in Fig. 10. After calcination, both Ni/SA and NiMn(0.25)/SA catalysts could be fitted with Ni-O (2.08 Å) and Ni-Ni (2.95 Å) shells that correspond to cubic NiO scattering paths (Fig. 10a). A slightly smaller second shell coordination number for NiMn(0.25)/SA (CN_{Ni-Ni} = 6.6) compared with Ni/SA (CN_{Ni-Ni} = 8.1) indicates that the oxidic crystallites formed on NiMn(0.25)/SA are smaller than those on Ni/SA. However, due to the similar backscattering properties of Ni and Mn, we cannot firmly establish the presence of a mixed NiMn-oxide phase from these data. After reduction (Fig. 10b), both catalysts show mainly a contribution at the metallic Ni-Ni bond distance (2.49 Å), with no contribution from oxygen originating from MnO within the first coordination shell. We can therefore conclude that Ni is present as metallic nanoparticles after reduction.

EXAFS spectra obtained on the Mn K-edge were background subtracted and fitted in Viper using single scattering paths of relevant candidate structures calculated with FEFF8. The k^2-weighted Fourier transformed EXAFS spectra of the Mn K-edge are plotted in R-space in Fig. 11a and Fig. 11b for calcined and reduced catalysts, respectively. The corresponding path distances and coordination numbers are presented in Table 5. Clear differences are observed in the structure of calcined catalysts. Contributions from 3 coordination shells were fitted for Mn/SA. The Mn-O (1.91 Å) and

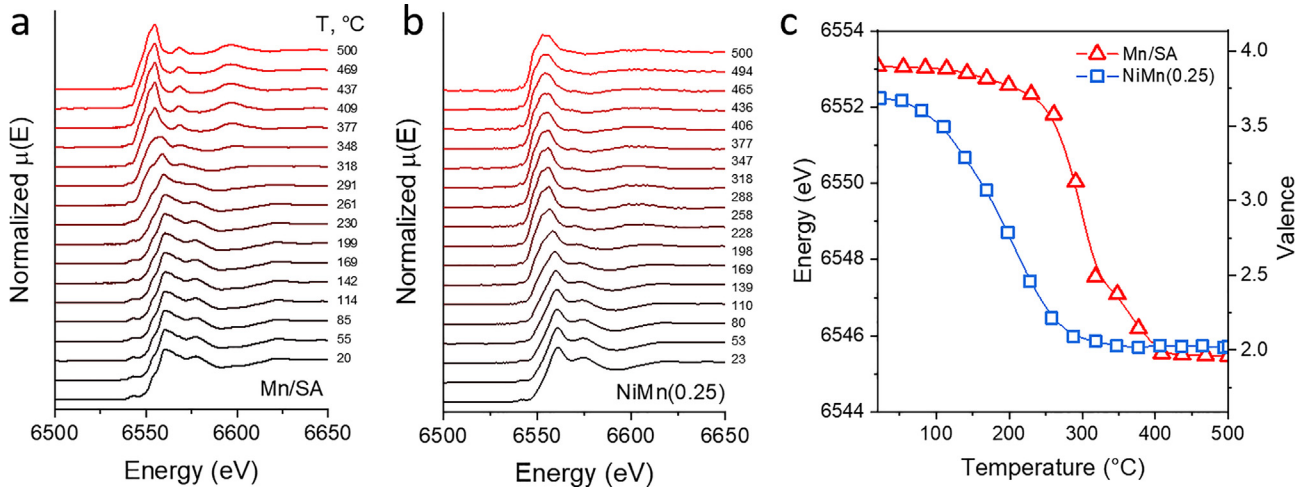

Fig. 9. Mn K-edge XANES spectra during catalyst reduction up to 500 °C for (a) Mn/SA and (b) NiMn(0.25)/SA. (c) Oxidation state determination of Mn using the half-edge energy.

Table 4
Fit parameters of k^3-weighted EXAFS spectra at the Ni K-edge.

Catalyst	Shell no.	Path	r (Å) [±]	CN [±]
Ni/SA (calcined)	1	Ni-O	2.06 [0.01]	5.8 [0.8]
	2	Ni-Ni	2.97 [0.01]	8.1 [1.6]
Ni/SA (reduced)	1	Ni-Ni	2.48 [0.01]	8.1 [0.6]
NiMn(0.25)/SA (calcined)	1	Ni-O	2.05 [0.01]	5.2 [0.6]
	2	Ni-Ni	2.98 [0.01]	6.6 [1.7]
NiMn(0.25)/SA (reduced)	1	Ni-Ni	2.48 [0.00]	8.5 [0.5]

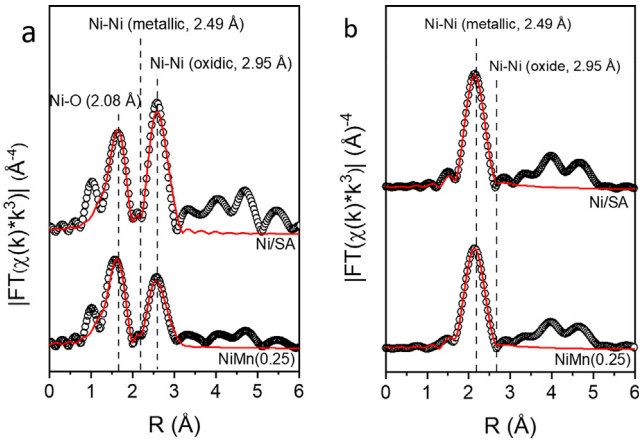

Fig. 10. (a) Ni K-edge Fourier transformed k^3-weighted EXAFS spectra of Ni/SA and NiMn(0.25)/SA after calcination at 350 °C. (b) Ni K-edge Fourier transformed k^3-weighted EXAFS spectra of Ni/SA and NiMn(0.25)/SA after reduction at 550 °C.

Mn-Mn (2.87 Å and 3.43 Å) bond distances and coordination numbers in calcined Mn/SA are consistent with the structure of β-MnO_2. This is in line with the XRD identification of the Mn-oxide phase. In contrast, NiMn(0.25)/SA exhibited only two coordination shells, which could be attributed to Mn-O (1.93 Å) and Mn-Mn (2.91 Å), although the latter scattering path may involve Ni as a backscatterer as well. Furthermore, the Mn-Mn contribution in NiMn(0.25)/SA has an intermediate bond length compared with the MnO_2 contributions observed in Mn/SA. Moreover, the $CN_{Mn\text{-}Mn}$ = 4.14 of NiMn(0.25)/SA is higher above that of the maximum degeneracy of 2 from Mn-Mn at 2.84 Å in bulk β-MnO_2. These results therefore indicate that Mn is likely present as a mixed NiMn oxide after calcination. Moreover, its presence in the mixed oxide facilitates the reduction of Mn, as followed from the XANES measurements and other characterization data.

Reduced Mn/SA was fitted using candidate MnO crystal structures. In the absence of Ni, Mn formed bulk MnO after reduction with coordination numbers of 4.7 (Mn-O, 2.23 Å) and 10.4 (Mn-Mn, 3.13 Å) determined for the first and second shell, respectively. Promoted catalysts exhibited a considerably lower Mn-O coordination number at 2.1, and only a small contribution from a second shell ($CN_{Mn\text{-}Mn}$ = 1.0). The second shell, assigned to a single scattering path of Mn-Mn at 3.60 Å, appeared at a considerably longer bond distance than that in Mn/SA. A minor contribution at around 2.50 Å could not be fitted. We nevertheless speculate that this may be the contribution from the backscattering of metallic Ni, originating from MnO species decorating metallic Ni particles.

Additional structural information for Mn was derived from the pre-edge features of Mn K-edge spectra. The pre-edge feature has been extensively studied for 3d transition metals and often relates to electronic transitions from 1s core levels to empty 3d levels, but the exact transition and pre-edge intensity depends on the symmetry of the absorbing 3d metal (e.g., octahedral *vs.* tetrahedral) [47]. Fig. 11c shows the pre-edge features of reduced Mn/SA, NiMn (0.25)/SA and a MnO reference, all of which have Mn in the +2 oxidation state as determined by their edge position. Clearly, Mn/SA and MnO have nearly identical pre-edge features, which can be attributed to the transition of the 1s electron to the 3d state in Mn located in octahedral (O_h) sites. In contrast, NiMn(0.25)/SA exhibits a more intense pre-edge feature, which can be assigned to Mn located in tetrahedral (T_d) sites [45]. We therefore infer that the Ni particles are decorated with MnO clusters, which are highly dispersed and in a lower coordination. The deviation in the coordination environment from Mn in cubic MnO is indicative of a more hexagonal-type structure of MnO. In our earlier work we deter-

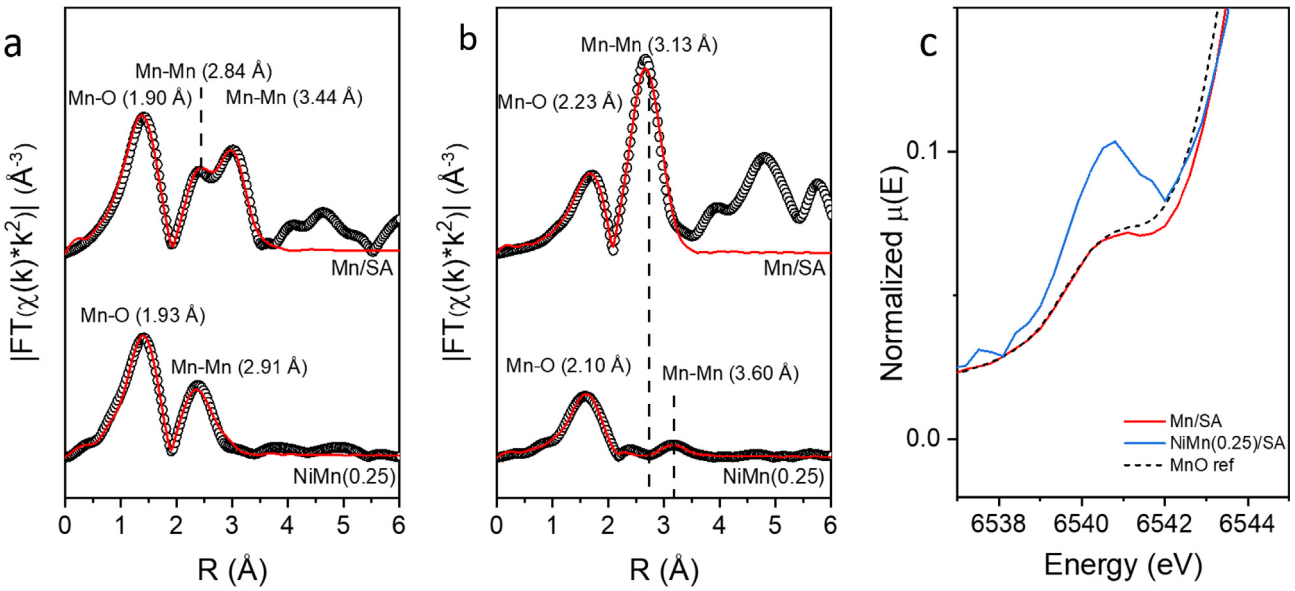

Fig. 11. (a) Mn K-edge Fourier transformed k^2-weighted EXAFS spectra of Mn/SA and NiMn(0.25)/SA after calcination at 350 °C. (b) Mn K-edge Fourier transformed k^2-weighted EXAFS spectra of Mn/SA and NiMn(0.25)/SA after reduction at 500 °C. (c) Mn pre-edge of reduced catalysts and MnO reference.

Table 5
Fit parameters of k^2-weighted EXAFS spectra at the Mn K-edge.

Catalyst	Shell no.	Path	r (Å) [±]	CN [±]
Mn/SA (calcined)	1	Mn-O	1.90 [0.01]	5.5 [0.0]
	2	Mn-Mn	2.88 [0.01]	1.9 [0.0]
	3	Mn-Mn	3.44 [0.01]	5.2 [0.3]
Mn/SA (reduced)	1	Mn-O	2.22 [0.01]	5.5 [0.0]
	2	Mn-Mn	3.13 [0.00]	10.5 [0.1]
NiMn (0.25)/SA (calcined)	1	Mn-O	1.93 [0.00]	4.0 [0.0]
	2	Mn-Mn	2.92 [0.00]	4.1 [0.1]
NiMn (0.25)/SA (reduced)	1	Mn-O	2.10 [0.00]	2.1 [0.0]
	2	Mn-Mn	3.60 [0.01]	1.0 [0.1]

mined a Mn_4O_4 cluster on a planar Ni(1 1 1) surface model to represent MnO decorating metallic Ni. The findings of the current work, therefore, support the presence of a distorted cluster with low Mn-Mn coordination and Mn in a non-octahedral oxygen coordination environment.

In situ and *operando* IR spectroscopy is a powerful method to gain molecular level understanding of how metal particle size [40], and support choice [48–50] influence the mechanism of CO_2 methanation over supported catalysts. Despite this, considerable disagreement exists about the exact mechanism of the Sabatier reaction over Ni-based catalysts. In general, two main pathways have been proposed: (i) CO_2 dissociation and subsequent hydrogenation of a CO intermediate *via* a carbide mechanism, and (ii) direct CO_2 hydrogenation towards CH_4 with consecutive hydrogenated intermediates (e.g. formate, formyl, and methoxy species) [48,51]. The CO intermediate may either be formed *via* direct CO_2 dissociation [50,52], or *via* formate species [53–56]. Comprehensive studies probing the influence of Mn in CO_2 hydrogenation are not available yet.

In order to elucidate how the interaction between the catalyst and CO_2 changes with Mn addition, Ni/SA and NiMn(0.25)/SA catalysts were exposed to 0–10 mbar CO_2 in a controlled-environment IR cell at 50 °C. Catalysts were reduced at 550 °C in flowing H_2 and evacuated at 300 °C prior to exposure to other gases. On Ni/SA (Fig. 12a), there is evidence for weak interaction of CO_2 with the support through observation of linearly adsorbed CO_2 (2344 cm^{-1}), as well as stronger interactions as bicarbonates from asymmetric ν_{as}(OCO) = 1646–1647 cm^{-1} and symmetric ν_s(OCO) = 1448–1443 cm^{-1} vibrations, formed through the reaction between CO_2 and surface hydroxyl groups [57]. A strong indication for CO_2 activation at a temperature as low as 50 °C was found from the observation of linear, bridged, and three-fold bridged carbonyl species (2017 cm^{-1}, 1907 cm^{-1}, 1844 cm^{-1}, respectively) [58].

An additional interaction between CO_2 and NiMn(0.25)/SA was observed by the appearance of a band at 1539 cm^{-1} (Fig. 12b), which can be attributed to monodentate carbonates on MnO [59]. Raising the temperature to 350 °C showed that the carbonates were bound more strongly than the bicarbonates (Figure S12, Supporting Information). As these carbonate species were not observed for Ni/SA, these strongly bound species must be associated with MnO. Recent studies showed that medium/moderate basic sites are beneficial for CO_2 methanation over supported Ni catalysts [50,60,61]. Moreover, the basicity of Mn-oxide can enhance CO_2 adsorption on Al_2O_3-supported catalysts for reforming and hydrogenation reactions [29,62]. In addition, bridged carbonyl species found at 1907 cm^{-1} and 1905 cm^{-1} for Ni/SA and NiMn(0.25)/SA, respectively, are more intense for the Mn-promoted catalyst. This difference implies a higher rate of CO_2 dissociation to CO on the NiMn catalyst.

Investigating these catalysts by IR spectroscopy under methanation conditions (H_2/CO_2 = 4) clearly shows the impact of Mn on CO_2 activation. Fig. 13 shows *in situ* IR spectra obtained during methanation between 50 and 350 °C. At 50 °C, the NiMn(0.25)/SA catalyst exhibited an asymmetric contribution from $Ni(CO)_3$

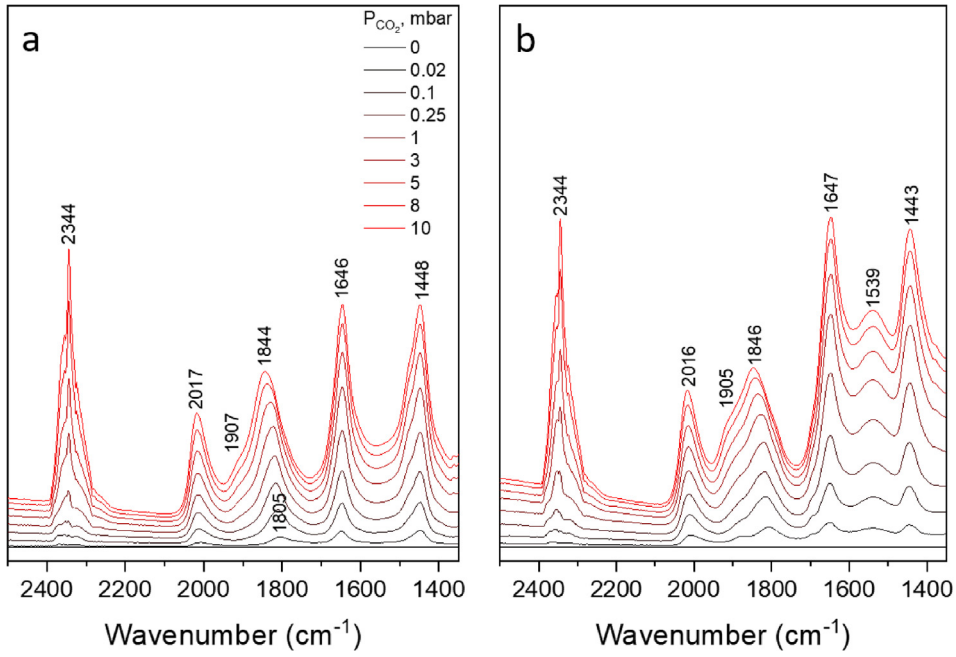

Fig. 12. Difference IR spectra during CO_2 pulsing between 0 and 10 mbar on (a) Ni/SA and (b) NiMn(0.25)/SA showing CO_2 adsorption.

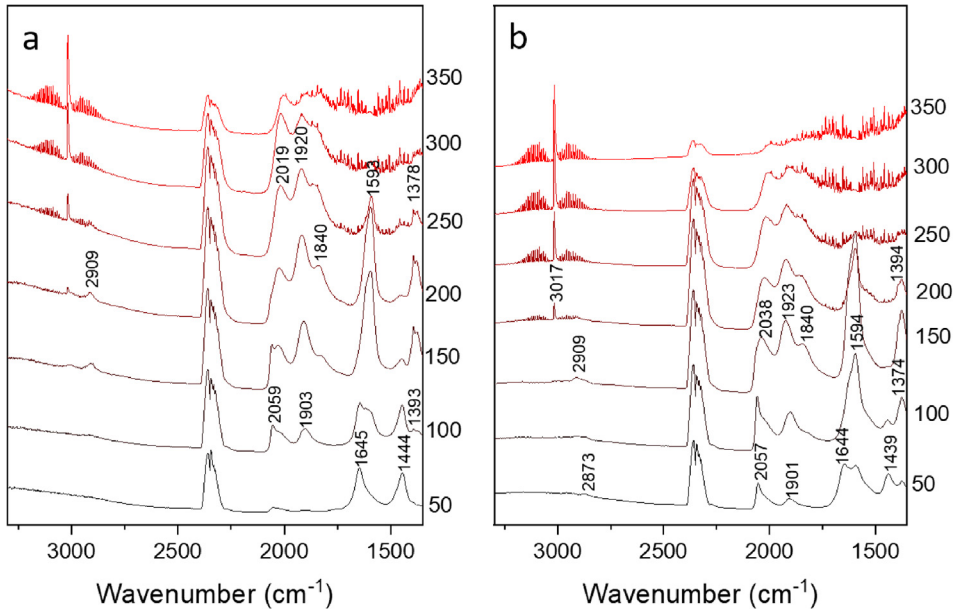

Fig. 13. *In situ* CO_2 methanation study in IR spectroscopy for (a) Ni/SA and (b) NiMn(0.25)/SA catalysts between 50 and 350 °C.

subcarbonyl species (2057 cm^{-1}) as well as bridged carbonyl species (1901 cm^{-1}) [63]. The presence of carbonyl species is significant at 50 °C on NiMn(0.25)/SA, in stark contrast to the Ni-only catalyst which requires higher temperatures in order to obtain a similar $Ni(CO)_3$ (2059 cm^{-1}) contribution. The fact that these carbonyl species are observed at higher wavenumbers during methanation in comparison to the CO_2 pulsing experiments indicates that the addition of H_2 significantly enhances the activation of CO_2 and formation of surface carbonyls. The shift is likely due to a higher CO coverage. Moreover, by comparing the relative contributions from (sub)carbonyl (>2000 cm^{-1}) species with those from bridged (<2000 cm^{-1}) species we clearly see that the NiMn(0.25)/SA catalyst has a larger proportion of (sub)carbonyls than Ni/SA, suggesting a larger build-up of CO on the Ni metal surface. These findings are consistent with the experimental and theoretical data obtained in our previous works, in which the presence of defective MnO clusters on the Ni nanoparticles enhanced CO_2 activation to yield CO adsorbed on the metallic Ni surface [32]. The role of H_2 could be the formation of oxygen defects in the Mn-oxide clusters.

Additional surface species were identified by IR spectroscopy during methanation. Below 100 °C, bicarbonates were observed on both catalysts from characteristic asymmetric and symmetric ν(OCO) vibrations at 1644 cm^{-1} and 1440 cm^{-1}, respectively. Formate species were observed only for the NiMn(0.25)/SA catalyst at 50 °C with typical stretching vibrations for ν(CH) = 2873 cm^{-1}, ν_{as}(OCO) = 1593 cm^{-1}, and ν_s(OCO) = 1374 cm^{-1}. Upon increasing

Table 6
SSITKA conversion, CH_4 selectivity, and surface residence times of reactants and products for Ni/SA and NiMn(0.25)/SA catalysts at 200 °C.

Catalyst	Mn/Ni	X_{CO2} (%)	S_{CH4} (%)	τCO_2 (s)	τCH_4 (s)
Ni/SA	0	2.1	99.5	2.4 ± 0.3	48 ± 5
NiMn(0.25)/SA	0.25	6.5	98.7	2.6 ± 0.3	30 ± 3

the temperature, formate bands increased on both catalysts at the expense of bicarbonate vibrations with the additional ν(CH) deformation mode vibration appearing around 1393 cm^{-1}. Furthermore, the ν(CH) stretching vibration on Ni/SA appeared at 2909 cm^{-1}, which is characteristic for formate adsorption on γ-Al_2O_3. As this feature is also observed for NiMn(0.25)/SA in addition to the stretching vibration ν(CH) = 2873 cm^{-1} typical for formates on MnO [64], we infer that formate species are present both on MnO and on Al_2O_3 regions of the support [50,57,65–68].

Clearly, the decomposition of formate species occurs at lower temperature on NiMn(0.25)/SA than on Ni/SA. Mechanistically, however, the relevance of formate species is still unclear for our catalysts. Earlier studies reported formate species to be reaction intermediates [48] and spectator species [40]. Steady-state isotopic transient kinetic analysis (SSITKA) is a powerful technique which allows for the measurement of surface residence times (τ) of species and intermediates under steady-state conditions, and may provide mechanistic insights into the role of these surface species when correlated with IR spectra [69].

Both Ni/SA and NiMn(0.25)/SA were studied with SSITKA at 200 °C to determine reactant and product residence times. Fig. 14 shows the normalized residual response of $^{12}CO_2$ and $^{12}CH_4$ after the isotopic switch from $^{12}CO_2/H_2/Ar$ to $^{13}CO_2/H_2/He$. The gas hold-up time was short (<4 s) as determined by the fast appearance of the He effluent gas (Fig. 14). The residence times of CO_2 and CH_4 were determined with respect to the He appearance (Table 6). Both catalysts have near identical $^{12}CO_2$ decay signals (Fig. 14 insert), which are slower than the decay of the effluent gas, indicating a weak and reversible interaction between CO_2 and the catalysts. In contrast, significant differences were observed in the $^{12}CH_4$ decay signals, with NiMn(0.25)/SA exhibiting a much faster decay than Ni/SA. The faster CH_4 decay for NiMn(0.25)/SA indicates a higher reactivity of surface intermediates than for Ni/SA. It is therefore likely that the enhanced CO_2 and CO dissociation prevent a build-up surface carbon species (*i.e.* CO) on the Ni surface of NiMn(0.25)/SA, resulting in a faster CH_4 decay. By contrast, the slower CO dissociation over Ni/SA results in a slower CH_4 decay. In addition, the IR spectra obtained at 200 °C for both catalysts (Fig. 13) showed notably higher formate contributions for Ni/SA than for NiMn(0.25)/SA. This indicates that formate species are likely not the primary intermediates in the methanation pathway of CO_2. Despite both catalysts yielding surface formates, the removal or decomposition of these species is more difficult on Ni/SA. If the formates behave as a reservoir, their increased stability over Mn-free catalysts contributes to the longer CH_4 transient. Similar to our work on TiO_2-supported Ni and NiMn systems, we therefore speculate that the promotional effect of Mn stems from more facile CO_2 and CO activation over highly dispersed and defective MnO-decorated Ni particles. Formate species may therefore act as a reservoir of adsorbed CO_2 rather than a primary reaction intermediate as evidenced by the CH_4 transient.

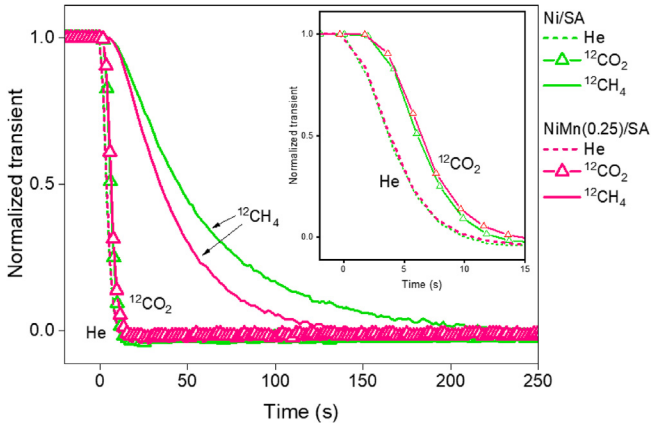

Fig. 14. Normalized mass spectrometer residual response of reactant ($^{12}CO_2$) and product ($^{12}CH_4$) in the effluent (He, inverted response) after steady-state isotopic switch over Ni/SA and NiMn(0.25)/SA at 200 °C. The inset shows the gas feed switch at 0 s from $^{12}CO_2/H_2/Ar$ to $^{13}CO_2/H_2/He$ (inverted He signal).

4. Conclusion

We investigated the influence of Mn on Ni/SiO_2-Al_2O_3 catalysts in CO_2 methanation. Our study shows that a higher Mn/Ni ratio leads to increased CO_2 and CO methanation activity. The higher catalytic activity is maintained during CO_2 methanation under 20 bar, with Mn-promoted catalysts also exhibiting superior stability and higher CH_4 selectivity at low temperatures. *Operando* XANES and EXAFS measurements combined with STEM-EDX mapping confirmed that active catalysts consisted of metallic Ni nanoparticles decorated with highly dispersed MnO with an intimate interaction between Ni and Mn already established prior to reduction. Mn facilitated the reduction of Ni during reduction and improved the Ni dispersion. In addition, CO_2 adsorption and activation occurred at lower temperature in the presence of Mn according to IR spectroscopy. Formate species were observed on both NiMn/SA and Ni/SA catalysts, but their exact role requires further investigation with supports that have a weaker interaction with CO_2. Nevertheless, the introduction of moderate basic sites from MnO appeared to be beneficial for the overall methanation activity. Our findings highlight the possibility of promoting Ni-based catalysts with a cheap and abundant transition metal like Mn for potential industrial applications in sustainable power-to-gas schemes.

Declaration of Competing Interest

The authors declared that there is no conflict of interest.

Acknowledgements

The authors acknowledge financial support from the Netherlands Organization for Scientific Research (NWO) and BASF for a TA-CHIPP grant. The authors thank the staff at the BM26A Dubble beamline at the ESRF (Grenoble, France) for the allocation of beam time (proposal no. 26-01-1166). We thank Tobias Kimpel, Valery Muravev, and Yujie Liu for their assistance during the XAFS beam time. We thank Mrs. Adelheid Elemans-Mehring for performing the elemental analysis. We thank Dr. Mengyue Wu and Dr. Frans Tichelaar for the STEM-EDX measurements performed at Delft University of Technology. We thank SASOL for providing the SIRAL20 catalyst support. Gabriella Garbarino acknowledges the University of Genova for financial support from the "Mobility

Program for Young Researchers 2017 and 2018" awarded to carry out research at TU/e.

Appendix A. Supplementary material

Additional catalyst characterization (STEM-EDX, XANES, EXAFS, IR) and kinetic data. to this article can be found online at https://doi.org/10.1016/j.jcat.2019.12.026.

References

[1] M. Götz, J. Lefebvre, F. Mörs, A. McDaniel Koch, F. Graf, S. Bajohr, R. Reimert, T. Kolb, Renewable power-to-gas: a technological and economic review, Renew. Energy. 85 1371–1390 (2016), https://doi.org/10.1016/j.renene.2015.07.066.

[2] G. Centi, E.A. Quadrelli, S. Perathoner, Catalysis for CO_2 conversion: a key technology for rapid introduction of renewable energy in the value chain of chemical industries, Energy Environ. Sci. 6 (2013) 1711–1731, https://doi.org/10.1039/C3EE00056G.

[3] B. Miao, S.S.K. Ma, X. Wang, H. Su, S.H. Chan, Catalysis mechanisms of CO_2 and CO methanation, Catal. Sci. Technol. 6 (2016) 4048–4058, https://doi.org/10.1039/C6CY00478D.

[4] Y.A. Daza, J.N. Kuhn, CO_2 conversion by reverse water gas shift catalysis: comparison of catalysts, mechanisms and their consequences for CO_2 conversion to liquid fuels, RSC Adv. 6 (2016) 49675–49691, https://doi.org/10.1039/C6RA05414E.

[5] J. Gao, Q. Liu, F. Gu, B. Liu, Z. Zhong, F. Su, Recent advances in methanation catalysts for the production of synthetic natural gas, RSC Adv. 5 (2015) 22759–22776, https://doi.org/10.1039/C4RA16114A.

[6] W. Wang, S. Wang, X. Ma, J. Gong, Recent advances in catalytic hydrogenation of carbon dioxide, Chem. Soc. Rev. 40 (2011) 3703–3727, https://doi.org/10.1039/C1CS15008A.

[7] W. Wei, G. Jinlong, Methanation of carbon dioxide: an overview, Front. Chem. Sci. Eng. 5 (2011) 2–10, https://doi.org/10.1007/s11705-010-0528-3.

[8] F. Solymosi, A. Erdohelyi, M. Kocsis, Methanation of CO2 on supported Ru catalysts, J. Chem. Soc. Faraday Trans. 1 Phys. Chem. Condens. Phases. 77 (1981) 1003–1012. doi:10.1039/F19817701003.

[9] G. Weatherbee, C.H. Bartholomew, Hydrogenation of CO2 on group VIII metals IV. Specific activities and selectivities of silica-supported Co, Fe, and Ru, J. Catal. 87 (1984) 352–362. doi:10.1016/0021-9517(84)90196-9.

[10] J.H. Kwak, L. Kovarik, J. Szanyi, CO_2 reduction on supported Ru/Al_2O_3 catalysts: cluster size dependence of product selectivity, ACS Catal. 3 (2013) 2449–2455, https://doi.org/10.1021/cs400381f.

[11] G. Garbarino, D. Bellotti, E. Finocchio, L. Magistri, G. Busca, Methanation of carbon dioxide on Ru/Al_2O_3: catalytic activity and infrared study, Catal. Today 277 (2016) 21–28, https://doi.org/10.1016/j.cattod.2015.12.010.

[12] L. Falbo, C.G. Visconti, L. Lietti, J. Szanyi, The effect of CO on CO_2 methanation over Ru/Al_2O_3 catalysts: a combined steady-state reactivity and transient DRIFT spectroscopy study, Appl. Catal. B Environ. 256 (2019), https://doi.org/10.1016/j.apcatb.2019.117791 117791.

[13] A. Bermejo-López, B. Pereda-Ayo, J.A. González-Marcos, J.R. González-Velasco, Mechanism of the CO_2 storage and in situ hydrogenation to CH_4. Temperature and adsorbent loading effects over $Ru\text{-}CaO/Al_2O_3$ and $Ru\text{-}Na_2CO_3/Al_2O_3$ catalysts, Appl. Catal. B Environ. 256 (2019), https://doi.org/10.1016/j.apcatb.2019.117845 117845.

[14] J. Gao, Y. Wang, Y. Ping, D. Hu, G. Xu, F. Gu, F. Su, A thermodynamic analysis of methanation reactions of carbon oxides for the production of synthetic natural gas, RSC Adv. 2 (2012) 2358–2368, https://doi.org/10.1039/C2RA00632D.

[15] S. Rönsch, J. Schneider, S. Matthischke, M. Schlüter, M. Götz, J. Lefebvre, P. Prabhakaran, S. Bajohr, Review on methanation – from fundamentals to current projects, Fuel 166 (2016) 276–296, https://doi.org/10.1016/j.fuel.2015.10.111.

[16] M.A.A. Aziz, A.A. Jalil, S. Triwahyono, A. Ahmad, CO_2 methanation over heterogeneous catalysts: recent progress and future prospects, Green Chem. 17 (2015) 2647–2663, https://doi.org/10.1039/C5GC00119F.

[17] S. De, J. Zhang, R. Luque, N. Yan, Ni-based bimetallic heterogeneous catalysts for energy and environmental applications, Energy Environ. Sci. 9 (2016) 3314–3347, https://doi.org/10.1039/C6EE02002J.

[18] J. Ren, X. Qin, J.-Z. Yang, Z.-F. Qin, H.-L. Guo, J.-Y. Lin, Z. Li, Methanation of carbon dioxide over $Ni–M/ZrO_2$ (M=Fe Co, Cu) catalysts: effect of addition of a second metal, Fuel Process. Technol. 137 (2015) 204–211, https://doi.org/10.1016/j.fuproc.2015.04.022.

[19] L.R. Winter, E. Gomez, B. Yan, S. Yao, J.G. Chen, Tuning Ni-catalyzed CO_2 hydrogenation selectivity via Ni-ceria support interactions and Ni-Fe bimetallic formation, Appl. Catal. B Environ. 224 (2018) 442–450, https://doi.org/10.1016/j.apcatb.2017.10.036.

[20] B.C. Enger, A. Holmen, Nickel and fischer-tropsch synthesis, Catal. Rev. 54 (2012) 437–488, https://doi.org/10.1080/01614940.2012.670088.

[21] A.Y. Khodakov, W. Chu, P. Fongarland, Advances in the development of novel cobalt fischer–tropsch catalysts for synthesis of long-chain hydrocarbons and clean fuels, Chem. Rev. 107 (2007) 1692–1744, https://doi.org/10.1021/cr050972v.

[22] F. Morales, F.M.F. de Groot, O.L.J. Gijzeman, A. Mens, O. Stephan, B.M. Weckhuysen, Mn promotion effects in Co/TiO_2 Fischer-tropsch catalysts as investigated by XPS and STEM-EELS, J. Catal. 230 (2005) 301–308, https://doi.org/10.1016/j.jcat.2004.11.047.

[23] F. Morales, F.M.F. de Groot, P. Glatzel, E. Kleimenov, H. Bluhm, M. Hävecker, A. Knop-Gericke, B.M. Weckhuysen, In Situ X-ray absorption of $Co/Mn/TiO_2$ catalysts for fischer–tropsch synthesis, J. Phys. Chem. B 108 (2004) 16201–16207, https://doi.org/10.1021/jp0403846.

[24] G.L. Bezemer, P.B. Radstake, U. Falke, H. Oosterbeek, H.P.C.E. Kuipers, A.J. van Dillen, K.P. de Jong, Investigation of promoter effects of manganese oxide on carbon nanofiber-supported cobalt catalysts for fischer-tropsch synthesis, J. Catal. 237 (2006) 152–161, https://doi.org/10.1016/j.jcat.2005.10.031.

[25] A. Zhao, W. Ying, H. Zhang, M. Hongfang, D. Fang, Ni/Al_2O_3 catalysts for syngas methanation: Effect of Mn promoter, J. Nat. Gas Chem. 21 (2012) 170–177, https://doi.org/10.1016/S1003-9953(11)60350-2.

[26] W.A. Wan Abu Bakar, R. Ali, N.S. Mohammad, The effect of noble metals on catalytic methanation reaction over supported Mn/Ni oxide based catalysts, Arab. J. Chem. 8 (2015) 632–643. doi:10.1016/j.arabjc.2013.06.009.

[27] K. Zhao, Z. Li, L. Bian, CO_2 methanation and co-methanation of CO and CO_2 over Mn-promoted Ni/Al_2O_3 catalysts, Front. Chem. Sci. Eng. 10 (2016) 273–280, https://doi.org/10.1007/s11705-016-1563-5.

[28] V. Shadravan, E. Kennedy, M. Stockenhuber, An experimental investigation on the effects of adding a transition metal to Ni/Al_2O_3 for catalytic hydrogenation of CO and CO_2 in presence of light alkanes and alkenes, Catal. Today 307 (2018) 277–285, https://doi.org/10.1016/j.cattod.2017.05.036.

[29] T. Burger, F. Koschany, O. Thomys, K. Köhler, O. Hinrichsen, CO_2 methanation over Fe- and Mn-promoted co-precipitated Ni-Al catalysts: Synthesis, characterization and catalysis study, Appl. Catal. A Gen. 558 (2018) 44–54, https://doi.org/10.1016/j.apcata.2018.03.021.

[30] T. Burger, F. Koschany, A. Wennig, O. Thomys, K. Köhler, O. Hinrichsen, Simultaneous activity and stability increase of co-precipitated Ni–Al CO_2 methanation catalysts by synergistic effects of Fe and Mn promoters, Catal. Sci. Technol. 8 (2018) 5920–5932, https://doi.org/10.1039/C8CY01834K.

[31] G. Garbarino, S. Chitsazan, T.K. Phung, P. Riani, G. Busca, Preparation of supported catalysts: a study of the effect of small amounts of silica on Ni/Al_2O_3 catalysts, Appl. Catal. A Gen. 505 (2015) 86–97, https://doi.org/10.1016/j.apcata.2015.07.017.

[32] W.L. Vrijburg, E. Moioli, W. Chen, M. Zhang, B.J.P. Terlingen, B. Zijlstra, I.A.W. Filot, A. Züttel, E.A. Pidko, E.J.M. Hensen, Efficient base-metal $NiMn/TiO_2$ catalyst for CO_2 methanation, ACS Catal. 9 (2019) 7823–7839, https://doi.org/10.1021/acscatal.9b01968.

[33] B. Ravel, M. Newville, ATHENA, ARTEMIS, HEPHAESTUS : data analysis for X-ray absorption spectroscopy using IFEFFIT, J. Synchrotron Radiait. 12 (2005) 537–541, https://doi.org/10.1107/S0909049505012719.

[34] L. van Haandel, E.J.M. Hensen, T. Weber, High pressure flow reactor for in situ X-ray absorption spectroscopy of catalysts in gas-liquid mixtures—A case study on gas and liquid phase activation of a $Co\text{-}Mo/Al_2O_3$ hydrodesulfurization catalyst, Catal. Today 292 (2017) 51–57, https://doi.org/10.1016/j.cattod.2016.08.027.

[35] W. Chen, R. Pestman, B. Zijlstra, I.A.W. Filot, E.J.M. Hensen, Mechanism of cobalt-catalyzed CO hydrogenation: 1, Methanation, ACS Catal. 7 (2017) 8050–8060, https://doi.org/10.1021/acscatal.7b02757.

[36] B.W. Hoffer, A. Dick van Langeveld, J.-P. Janssens, R.L.C. Bonné, C.M. Lok, J.A. Moulijn, Stability of highly dispersed Ni/Al_2O_3 catalysts: effects of pretreatment, J. Catal. 192 (2000) 432–440, https://doi.org/10.1006/jcat.2000.2867.

[37] B. Scheffer, P. Molhoek, J.A. Moulijn, Temperature-programmed reduction of $NiOWO_3/Al_2O_3$ hydrodesulphurization catalysts, Appl. Catal. 46 (1989) 11–30, https://doi.org/10.1016/S0166-9834(00)81391-3.

[38] P. Kim, Y. Kim, H. Kim, I.K. Song, J. Yi, Synthesis and characterization of mesoporous alumina with nickel incorporated for use in the partial oxidation of methane into synthesis gas, Appl. Catal. A Gen. 272 (2004) 157–166, https://doi.org/10.1016/j.apcata.2004.05.055.

[39] B.R. Strohmeier, D.M. Hercules, Surface spectroscopic characterization of manganese/aluminum oxide catalysts, J. Phys. Chem. 88 (1984) 4922–4929, https://doi.org/10.1021/j150665a026.

[40] C. Vogt, E. Groeneveld, G. Kamsma, M. Nachtegaal, L. Lu, C.J. Kiely, P.H. Berben, F. Meirer, B.M. Weckhuysen, Unravelling structure sensitivity in CO_2 hydrogenation over nickel, Nat. Catal. 1 (2018) 127–134, https://doi.org/10.1038/s41929-017-0016-y.

[41] D. Beierlein, D. Häussermann, M. Pfeifer, T. Schwarz, K. Stöwe, Y. Traa, E. Klemm, Is the CO_2 Methanation on Highly Loaded $Ni\text{-}Al_2O_3$ Catalysts Really Structure-Sensitive?, Appl. Catal. B Environ. (2018), https://doi.org/10.1016/j.apcatb.2018.12.064.

[42] K. Jalama, Carbon dioxide hydrogenation over nickel-, ruthenium-, and copper-based catalysts: review of kinetics and mechanism, Catal. Rev. 59 (2017) 95–164, https://doi.org/10.1080/01614940.2017.1316172.

[43] R. Mutschler, E. Moioli, W. Luo, N. Gallandat, A. Züttel, CO_2 hydrogenation reaction over pristine Fe Co, Ni, Cu and Al_2O_3 supported Ru: comparison and determination of the activation energies, J. Catal. 366 (2018) 139–149, https://doi.org/10.1016/j.jcat.2018.08.002.

[44] E. Chalmin, F. Farges, G.E. Brown, A pre-edge analysis of Mn K-edge XANES spectra to help determine the speciation of manganese in minerals and glasses, Contrib. Mineral. Petrol. 157 (2009) 111–126, https://doi.org/10.1007/s00410-008-0323-z.

[45] F. Farges, Ab initio and experimental pre-edge investigations of the Mn K -edge XANES in oxide-type materials, Phys. Rev. B. 71 (2005), https://doi.org/10.1103/PhysRevB.71.155109 155109.

[46] K. Nam, M.G. Kim, K. Kim, In situ Mn K-edge X-ray Absorption spectroscopy studies of electrodeposited manganese oxide films for electrochemical capacitors, J. Phys. Chem. C 111 (2007) 749–758, https://doi.org/10.1021/jp063130o.
[47] T. Yamamoto, Assignment of pre-edge peaks in K-edge x-ray absorption spectra of 3d transition metal compounds: electric dipole or quadrupole?, X-Ray Spectrom. 37 (2008) 572–584, https://doi.org/10.1002/xrs.1103.
[48] P.A.U. Aldana, F. Ocampo, K. Kobl, B. Louis, F. Thibault-Starzyk, M. Daturi, P. Bazin, S. Thomas, A.C. Roger, Catalytic CO_2 valorization into CH_4 on Ni-based ceria-zirconia. Reaction mechanism by operando IR spectroscopy, Catal. Today 215 (2013) 201–207, https://doi.org/10.1016/j.cattod.2013.02.019.
[49] Q. Pan, J. Peng, S. Wang, S. Wang, In situ FTIR spectroscopic study of the CO_2 methanation mechanism on $Ni/Ce_{0.5}Zr_{0.5}O_2$, Catal. Sci. Technol. 4 (2014) 502–509, https://doi.org/10.1039/C3CY00868A.
[50] H. Muroyama, Y. Tsuda, T. Asakoshi, H. Masitah, T. Okanishi, T. Matsui, K. Eguchi, Carbon dioxide methanation over Ni catalysts supported on various metal oxides, J. Catal. 343 (2016) 178–184, https://doi.org/10.1016/j.jcat.2016.07.018.
[51] A. Solis-Garcia, J.F. Louvier-Hernandez, A. Almendarez-Camarillo, J.C. Fierro-Gonzalez, Participation of surface bicarbonate, formate and methoxy species in the carbon dioxide methanation catalyzed by ZrO_2-supported Ni, Appl. Catal. B Environ. 218 (2017) 611–620, https://doi.org/10.1016/j.apcatb.2017.06.063.
[52] A. Karelovic, P. Ruiz, Mechanistic study of low temperature CO_2 methanation over Rh/TiO_2 catalysts, J. Catal. 301 (2013) 141–153, https://doi.org/10.1016/j.jcat.2013.02.009.
[53] M.A.A. Aziz, A.A. Jalil, S. Triwahyono, R.R. Mukti, Y.H. Taufiq-Yap, M.R. Sazegar, Highly active Ni-promoted mesostructured silica nanoparticles for CO_2 methanation, Appl. Catal. B Environ. 147 (2014) 359–368, https://doi.org/10.1016/j.apcatb.2013.09.015.
[54] X. Wang, Y. Hong, H. Shi, J. Szanyi, Kinetic modeling and transient DRIFTS–MS studies of CO_2 methanation over Ru/Al_2O_3 catalysts, J. Catal. 343 (2016) 185–195, https://doi.org/10.1016/j.jcat.2016.02.001.
[55] M. Marwood, R. Doepper, A. Renken, In-situ surface and gas phase analysis for kinetic studies under transient conditions the catalytic hydrogenation of CO_2, Appl. Catal. A Gen. 151 (1997) 223–246, https://doi.org/10.1016/S0926-860X(96)00267-0.
[56] H.C. Wu, Y.C. Chang, J.H. Wu, J.H. Lin, I.K. Lin, C.S. Chen, Methanation of CO_2 and reverse water gas shift reactions on Ni/SiO_2 catalysts: the influence of particle size on selectivity and reaction pathway, Catal. Sci. Technol. 5 (2015) 4154–4163, https://doi.org/10.1039/C5CY00667H.
[57] G. Busca, V. Lorenzelli, Infrared spectroscopic identification of species arising from reactive adsorption of carbon oxides on metal oxide surfaces, Mater. Chem. 7 (1982) 89–126, https://doi.org/10.1016/0390-6035(82)90059-1.
[58] S. Fujita, M. Nakamura, T. Doi, N. Takezawa, Mechanisms of methanation of carbon dioxide and carbon monoxide over nickel/alumina catalysts, Appl. Catal. A Gen. 104 (1993) 87–100, https://doi.org/10.1016/0926-860X(93)80212-9.
[59] J.I.I. Di Cosimo, V.K.K. Díez, M. Xu, E. Iglesia, C.R.R. Apesteguía, Structure and Surface and Catalytic Properties of Mg-Al Basic Oxides, J. Catal. 178 (1998) 499–510. doi:10.1006/jcat.1998.2161.**
[60] Q. Pan, J. Peng, T. Sun, S. Wang, S. Wang, Insight into the reaction route of CO_2 methanation: promotion effect of medium basic sites, Catal. Commun. 45 (2014) 74–78, https://doi.org/10.1016/j.catcom.2013.10.034.
[61] G. Garbarino, C. Wang, T. Cavattoni, E. Finocchio, P. Riani, M. Flytzani-Stephanopoulos, G. Busca, A study of $Ni/La\text{-}Al_2O_3$ catalysts: a competitive system for CO_2 methanation, Appl. Catal. B Environ. 248 (2019) 286–297, https://doi.org/10.1016/j.apcatb.2018.12.063.
[62] S.-H. Seok, S.H. Choi, E.D. Park, S.H. Han, J.S. Lee, Mn-promoted Ni/Al_2O_3 catalysts for stable carbon dioxide reforming of methane, J. Catal. 209 (2002) 6–15, https://doi.org/10.1006/jcat.2002.3627.
[63] M. Agnelli, H.M. Swaan, C. Marquez-Alvarez, G.A. Martin, C. Mirodatos, CO Hydrogenation on a nickel catalyst, J. Catal. 175 (1998) 117–128, https://doi.org/10.1006/jcat.1998.1978.
[64] M. Kantcheva, M.U. Kucukkal, S. Suzer, Spectroscopic investigation of species arising from CO chemisorption on titania-supported manganese, J. Catal. 190 (2000) 144–156, https://doi.org/10.1006/jcat.1999.2757.
[65] R.A.D. Betta, M. Shelef, Heterogeneous methanation: in situ infrared spectroscopic study of $RuAl_2O_3$ during the hydrogenation of CO, J. Catal. 48 (1977) 111–119, https://doi.org/10.1016/0021-9517(77)90082-3.
[66] A. Karelovic, P. Ruiz, CO_2 hydrogenation at low temperature over $Rh/\gamma\text{-}Al_2O_3$ catalysts: effect of the metal particle size on catalytic performances and reaction mechanism, Appl. Catal. B Environ. 113–114 (2012) 237–249, https://doi.org/10.1016/j.apcatb.2011.11.043.
[67] F. Solymosi, A. Erdöhelyi, M. Kocsis, Surface interaction between H_2 and CO_2 on $RhAl_2O_3$, studied by adsorption and infrared spectroscopic measurements, J. Catal. 65 (1980) 428–436, https://doi.org/10.1016/0021-9517(80)90319-X.
[68] G. Ramis, G. Busca, V. Lorenzelli, Low-temperature CO2 adsorption on metal oxides: spectroscopic characterization of some weakly adsorbed species, Mater. Chem. Phys. 29 (1991) 425–435, https://doi.org/10.1016/0254-0584(91)90037-U.
[69] X. Wang, H. Shi, J. Szanyi, Controlling selectivities in CO_2 reduction through mechanistic understanding, Nat. Commun. 8 (2017) 513, https://doi.org/10.1038/s41467-017-00558-9.